Journal of Investigations on Engineering & Technology
Volume 8, Issue 1, 17-33, 2025
ISSN: 2687-3052

Research Article

Application of Principal Component Analysis to ASTER Data for Hydrothermal Alteration Mapping in the Gümüşhane–Aktutan Region

Mustafa CEYLAN[1], Gökhan KÜLEKÇİ[2]

(Alınış / Received: 13.12.2025, Kabul / Accepted: 25.12.2025, Online Yayınlanma / Published Online: 31.12.2025)

Application of Principal Component Analysis to ASTER Data for Hydrothermal Alteration Mapping in the Gümüşhane–Aktutan Region

Keywords
ASTER
Principal Component Analysis (PCA)
Hydrothermal Alteration
Remote Sensing
Complex Tectonic Terrains

Abstract: Hydrothermal alteration mapping plays a fundamental role in mineral exploration and geological interpretation, particularly in regions with complex tectonic and mineralization settings. This study applies Principal Component Analysis (PCA) to Advanced Spaceborne Thermal Emission and Reflection Radiometer (ASTER) data to delineate hydrothermal alteration zones in the Gümüşhane–Aktutan area, Northeastern Türkiye. The workflow included radiometric calibration, atmospheric correction using the IAR Reflectance Correction method, and band stacking of VNIR, SWIR, and TIR datasets. Alteration indices were generated through band ratio techniques, followed by PCA to enhance spectral signatures of key minerals such as quartz, sericite, kaolinite, and advanced argillic phases. Eigenvalue analysis guided the selection of optimal band combinations, which were visualized using RGB composites to characterize alteration patterns. The results highlight PCA's effectiveness in differentiating overlapping spectral responses, enabling the identification of mixed alteration zones where multiple minerals coexist.

This research demonstrates that PCA-based integration of multispectral ASTER data provides a reliable and cost-efficient approach for hydrothermal alteration mapping in geologically intricate terrains. The study offers an original case-specific implementation of selective PCA, presenting novel insights into the mineralogical framework of the Gümüşhane–Aktutan region. Beyond confirming the potential of ASTER data for hydrothermal system detection, the findings emphasize the value of multivariate statistical methods in refining alteration mapping. Future work will integrate hyperspectral datasets, field validation, and machine learning-based classification to further enhance mapping precision. The originality of this contribution lies in adapting PCA methodology to ASTER data in a mineral-rich yet underexplored area, offering significant implications for regional exploration strategies and remote sensing applications in geology.

[1] Gümüşhane University, Department of Geomatics Engineering, 29000, Gümüşhane / TÜRKİYE
[2] Gümüşhane University, Department of Mining Engineering, 29000, Gümüşhane / TÜRKİYE
Corresponding Author and e-mail : Mustafa CEYLAN / mustafaceylan@gumushane.edu.tr

1. Introduction

Remote sensing technologies have become an indispensable component of mineral exploration, providing cost-effective and spatially extensive means of delineating hydrothermal alteration zones. Hydrothermal alteration serves as a fundamental indicator of mineralization processes, particularly within orogenic and volcanic–plutonic complexes, where alteration halos frequently coincide with zones of economic mineralization [1]. Among the various satellite datasets available, the Advanced Spaceborne Thermal Emission and Reflection Radiometer (ASTER) has proven especially valuable due to its spectral sensitivity across the visible–near infrared (VNIR), short-wave infrared (SWIR), and thermal infrared (TIR) regions. These spectral regions are diagnostically significant for identifying hydroxyl-bearing and silica-rich minerals such as kaolinite, sericite, and chlorite, which are characteristic of hydrothermal systems [2][3] [4].

The application of Principal Component Analysis (PCA) to multispectral data has long been recognized for its ability to enhance subtle spectral variations, suppress redundant information, and isolate alteration-related signals. The Crosta PCA approach, in particular, allows selective extraction of mineralogical information by maximizing variance within specific wavelength ranges that correspond to diagnostic absorption features [3]. Studies in regions such as the Eastern Desert of Egypt, the Iranian Volcanic Belt, and the Central Cameroon Domain have demonstrated the ability of ASTER-based PCA to discriminate between overlapping alteration zones and lithological units, providing a valuable template for exploration in geologically complex terrains [4][5]. Moreover, the integration of PCA with spectral band ratios, minimum noise fraction (MNF) transformation, and spectral unmixing has been shown to significantly enhance the detectability of subtle or mixed alteration zones [6][7].

Recent developments in mineral prospectivity modeling further emphasize the power of multivariate statistical methods in predictive exploration. The fusion of multispectral, geophysical, and geochemical datasets has enabled more robust delineation of mineralized targets. For instance, PCA applied to ASTER imagery in combination with aeromagnetic or radiometric data has successfully delineated alteration halos associated with base and precious metal systems in Nigeria and Sudan [8-10]. Despite these advancements, significant challenges remain in the discrimination of overlapping spectral signatures in regions with complex lithological assemblages and varied alteration types. This limitation underscores the need for selective and adaptive PCA methods capable of enhancing mineralogical contrasts within multispectral datasets.

Within this global framework, the Gümüşhane–Aktutan region of Northeastern Türkiye provides an ideal case for methodological testing. The area represents a tectonically intricate and mineral-rich segment of the Eastern Pontides Orogenic Belt, yet remains underexplored through advanced remote sensing approaches. Despite the recognition of its hydrothermal potential, a systematic PCA-based mapping study integrating radiometric calibration, IAR atmospheric correction, and eigenvalue-guided band selection has not been previously undertaken. The originality of this research lies in its adaptation of PCA to ASTER data to enhance the detection of hydrothermal alteration zones within complex tectonic settings. By applying a selective PCA workflow tailored to the spectral behavior of diagnostic minerals, this study addresses an existing gap in the literature concerning the optimization of multispectral data analysis for mineral exploration.

Ultimately, the study demonstrates that PCA-based enhancement can effectively differentiate overlapping alteration zones, offering a transferable methodological framework for similar geological contexts worldwide. The results presented herein contribute both methodologically and regionally to the growing field of remote sensing–assisted mineral exploration and the application of multivariate analysis in geological interpretation.

2. Study Area

The study area is located in the Aktutan region of the Gümüşhane province, Northeastern Türkiye, situated within the southern domain of the Eastern Pontides Orogenic Belt (EPOB), a major metallogenic province of the circum-Mediterranean orogenic system. The EPOB comprises an extensive succession of Mesozoic to Cenozoic volcanic and plutonic rocks, emplaced during multiple magmatic and tectonic episodes associated with subduction, collision, and post-collisional extensional processes [11, 12]. The local lithological framework predominantly consists of dacitic to rhyodacitic volcanic rocks, volcaniclastics, and tonalite–granodiorite intrusions, forming a favorable geochemical and structural environment for hydrothermal alteration.

Hydrothermal alteration in the Aktutan area is closely related to fault-controlled fluid flow, magmatic intrusions, and late-stage dike systems. Field and remote sensing observations indicate a zoned distribution of alteration minerals including advanced argillic, sericitic, propylitic, and kaolinite-rich assemblages, each reflecting variations

in thermal gradients, fluid chemistry, and permeability conditions [12-15] Among these, sericitic and quartz–sericitic assemblages are particularly developed along major fault zones, suggesting repeated fluid circulation and prolonged hydrothermal activity.

The Eastern Pontides host numerous Cu–Pb–Zn–Au deposits, many of which are genetically related to Paleocene–Eocene magmatic–hydrothermal systems [11, 14, 16]. These deposits exhibit well-defined alteration halos that are spectrally detectable using ASTER's SWIR and TIR sensors. The geological setting thus provides an ideal natural laboratory for testing PCA-based alteration mapping techniques. The area's lithological diversity, spectral sensitivity to alteration minerals, and relatively sparse vegetation cover collectively make it suitable for spectral analysis and statistical enhancement methods.

In this study, ASTER L1T imagery was used to delineate hydrothermal alteration zones within the region. The study area boundary was defined in Google Earth and refined in ArcGIS using shapefile conversion (Fig.1).

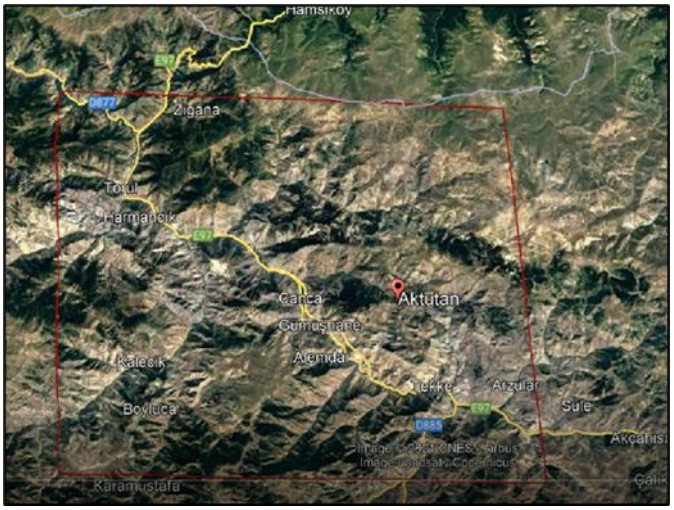

Figure 1. Location map of the study area within the Eastern Pontides Orogenic Belt

The subsequent analysis leveraged VNIR, SWIR, and TIR bands to map alteration assemblages including quartz, sericite, kaolinite, and advanced argillic minerals.

3. Data and Methods

3.1. Data Acquisition

The dataset used in this study consists of Advanced Spaceborne Thermal Emission and Reflection Radiometer (ASTER) Level 1T imagery obtained from the USGS EarthExplorer platform. The study area boundary was initially delineated in Google Earth Pro as a polygon (KML format), defining the extent of the Aktutan region within the Gümüşhane province. This boundary was subsequently converted to a shapefile in ArcGIS to ensure compatibility with ENVI software for subsequent image processing.

ASTER, a multispectral imaging instrument aboard NASA's Terra satellite, provides high-quality data across 14 spectral bands, encompassing three spectral subsystems: the Visible and Near-Infrared (VNIR), the Short-Wave Infrared (SWIR), and the Thermal Infrared (TIR) regions. These bands collectively cover the 0.52–11.65 μm wavelength range and offer distinct spatial resolutions optimized for mineralogical discrimination. Specifically, the VNIR subsystem includes three bands (bands 1–3) with a spatial resolution of 15 m, sensitive to iron oxides and ferric minerals. The SWIR subsystem, comprising bands 4–9 at 30 m resolution, captures diagnostic absorption features associated with hydroxyl-bearing minerals such as sericite, kaolinite, alunite, and chlorite. The TIR subsystem, composed of bands 10–14 with 90 m resolution, is sensitive to silicate and carbonate compositions, providing critical information on lithological variations [17, 18, 19].

To ensure complete SWIR spectral coverage, image acquisition was restricted to scenes collected between 2002 and 2007, since the SWIR detectors on the ASTER instrument ceased functioning after April 2008. The selection criteria prioritized imagery with minimal cloud cover (<10%) and low vegetation density, conditions known to improve the reliability of reflectance-based mineral detection [20, 29]. Daytime acquisitions were also favored to maximize radiometric contrast across surface materials.

The chosen ASTER L1T product provides radiometrically and geometrically corrected data, making it suitable for reflectance conversion and atmospheric correction workflows. The image metadata were recorded to ensure reproducibility. The acquisition and initial preprocessing workflow are summarized in Figure 2, while Figure 1 provides the geographic context of the study area.

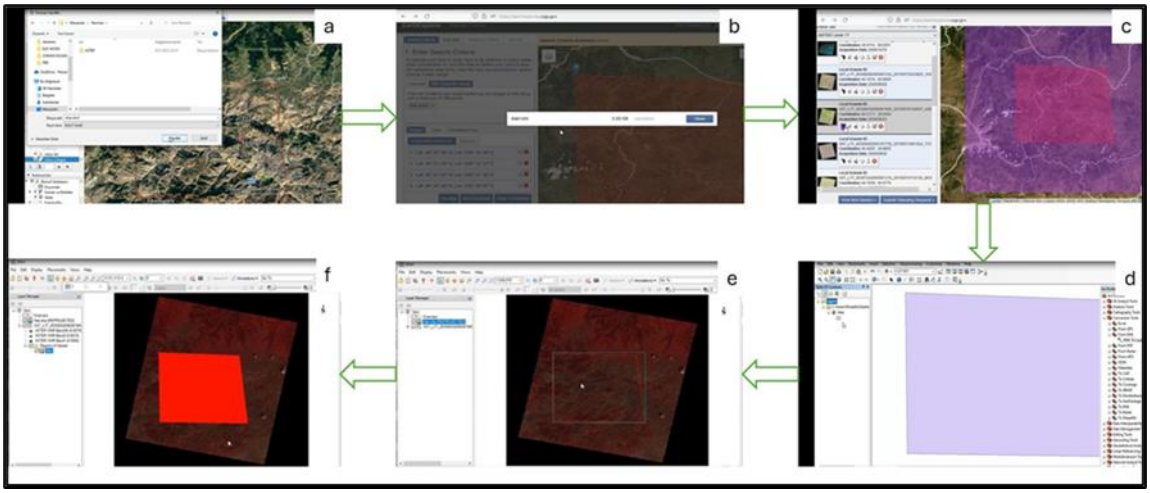

Figure 2. Flowchart showing data acquisition steps of study area delineation in: a) Drawing and saving the study area in Google Earth, b) Uploading the study area as kml in EarthExplorer, c) Downloading the satellite image corresponding to the study area from USGS, d) Converting the study area border in kml format to shp format, e) Opening the ASTER satellite image with the study area, f) Final determination of the work area

ASTER's spectral and spatial characteristics make it particularly suitable for hydrothermal alteration mapping because its SWIR bands effectively capture absorption features around 2.2 μm (Al–OH) and 2.33 μm (Mg–OH), which correspond to key alteration minerals such as kaolinite, illite, chlorite, and sericite [22, 23] (Table 1).

Table 1. Summary of ASTER sensor characteristics including wavelength range, spectral coverage, and spatial resolution for each subsystem [45]

Subsystem	Band No.	Spectral Range (μm)	Spatial Resolution (m)	Quantization Levels
VNIR	1	0.52-0.60	15	8 bits
VNIR	2	0.63-0.69	15	8 bits
VNIR	3N	0.78-0.86	15	8 bits
VNIR	3B	0.78-0.86	15	8 bits
SWIR	4	1.60-1.70	30	8 bits
SWIR	5	2.145-2.185	30	8 bits
SWIR	6	2.185-2.225	30	8 bits
SWIR	7	2.235-2.285	30	8 bits
SWIR	8	2.295-2.365	30	8 bits
SWIR	9	2.360-2.430	30	8 bits
TIR	10	8.125-8.475	90	12 bits
TIR	11	8.475-8.825	90	12 bits
TIR	12	8.925-9.275	90	12 bits
TIR	13	10.25-10.95	90	12 bits
TIR	14	10.95-11.65	90	12 bits

3.2. Preprocessing

Prior to the application of multivariate statistical analyses, the ASTER Level 1T imagery underwent a series of preprocessing steps designed to convert the raw Digital Number (DN) values into physically meaningful surface reflectance and emissivity data. These preprocessing operations were performed using ENVI 5.3 and ArcGIS Pro 10.8, following established protocols for geological remote sensing [18, 22, 24]. The overall preprocessing workflow is illustrated in Figure 3.

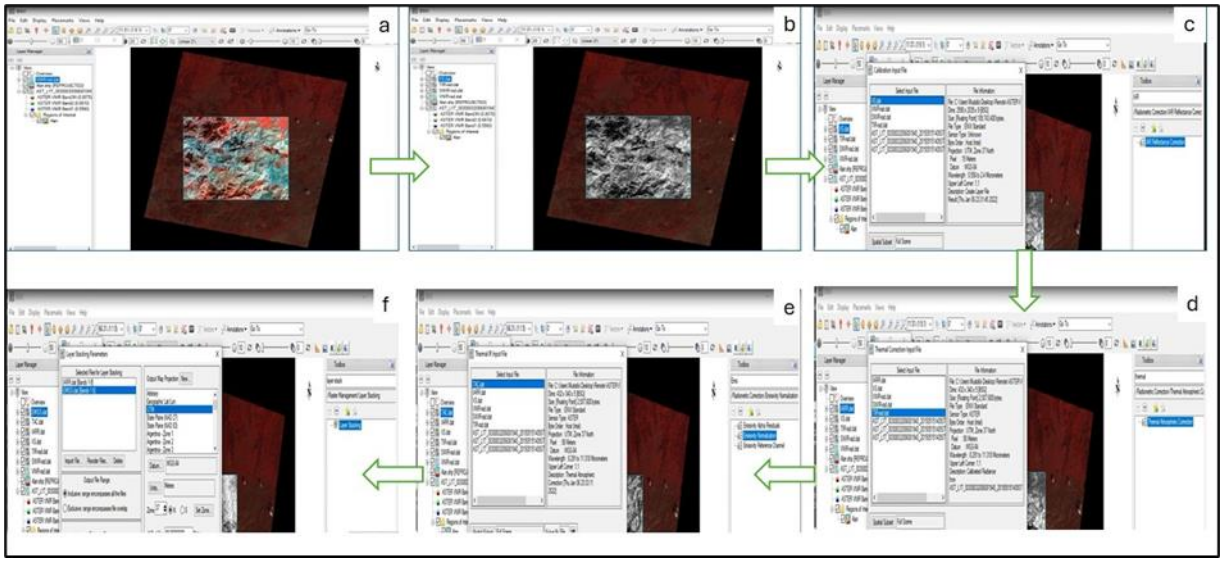

Figure 3. Preprocessing workflow diagram showing sequential steps: a) Radiometric calibration of the VNIR band, b) VNIR - SWIR layer stack, c) Applying IAR Reflectance Correction to layer stack d) Applying of Thermal Atmospheric Correction to TIR, e) Applying Emissivity Normalization to the TIR band with Thermal Atmospheric Correction applied, f) Layer stack for atmospherically corrected VNIR-SWIR and TIR bands

3.2.1. Radiometric Calibration

The first stage involved radiometric calibration, which converts DN values recorded by the satellite sensor into spectral radiance (Lλ) values using band-specific calibration coefficients derived from the image metadata. Radiometric calibration is essential for removing sensor-related distortions and standardizing pixel intensity across spectral bands [25].
The conversion is expressed mathematically as:

$$L_\lambda = (DN \times G) + O$$

where G represents the gain coefficient and O the offset value, both obtained from the ASTER metadata [17]. This step ensures that each pixel's digital response accurately corresponds to the intensity of radiation received at the sensor, facilitating subsequent conversion to reflectance.

The histogram reveals a compression of DN values after radiometric calibration, indicating improved normalization across the scene (Figure 4). This correction minimizes the effects of variable solar illumination and sensor gain, ensuring consistency among spectral bands [29].

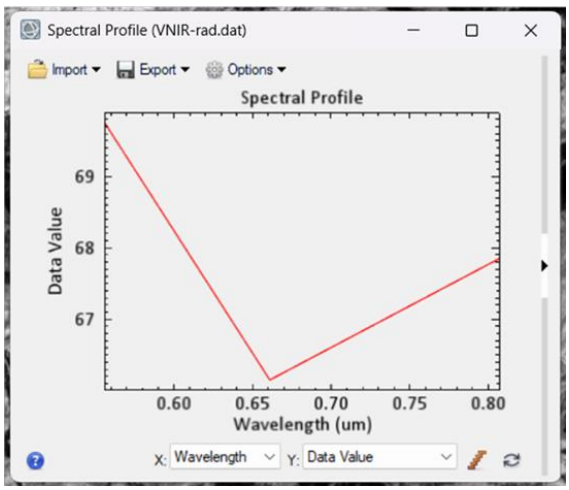

Figure 4. Example histogram of raw DN values before and after radiometric calibration for VNIR Band 2, demonstrating normalization and improved tonal balance

3.2.2. Conversion to Reflectance and Atmospheric Correction

Following calibration, the image was converted from spectral radiance to surface reflectance to remove atmospheric scattering and absorption effects caused by aerosols, water vapor, and molecular gases. For this study, the IAR (Internal Average Relative Reflectance) method was selected over the more commonly used FLAASH (Fast Line-of-sight Atmospheric Analysis of Spectral Hypercubes) correction, owing to the IAR method's superior performance in arid and semi-arid terrains with sparse vegetation [26, 27].

The IAR technique operates by normalizing each pixel's radiance to an average scene spectrum, effectively compensating for additive atmospheric effects without requiring detailed atmospheric modeling inputs. This approach is particularly advantageous for ASTER datasets where atmospheric profiles and ground calibration data are unavailable [28, 29].

After applying IAR correction, the absorption features near 2.2 μm (Al–OH) and 2.33 μm (Mg–OH) become more distinct, indicating the successful suppression of atmospheric scattering and the enhancement of diagnostic spectral signatures associated with sericite and chlorite (Figure 5). Similar observations have been reported in ASTER-based alteration studies [19, 24].

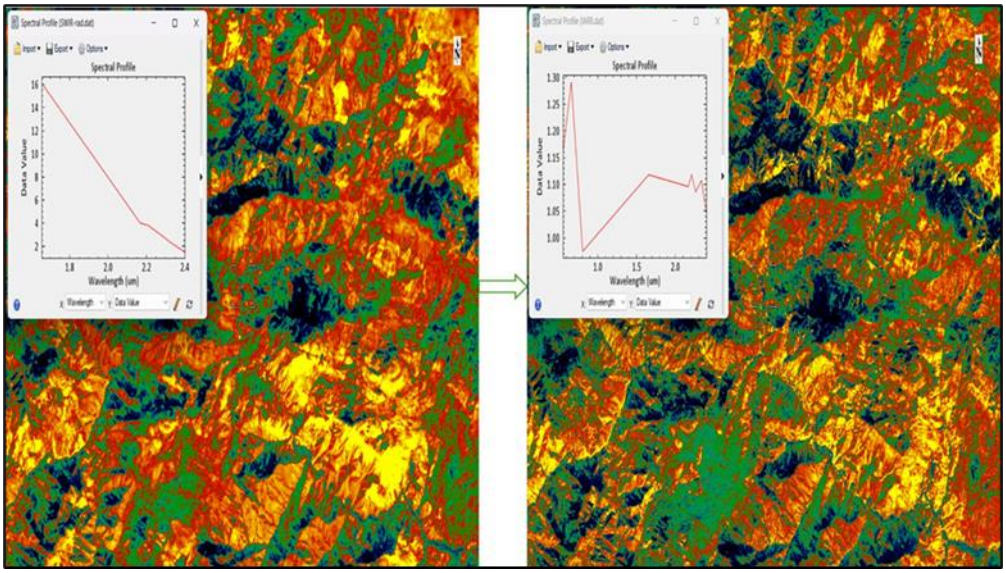

Figure 5. Comparative reflectance curves showing pre-correction radiance spectrum and post-IAR reflectance for representative pixels in SWIR Band 6 (2.205 μm), highlighting enhanced mineral absorption features.

3.2.3. Emissivity Normalization for TIR Bands

For the Thermal Infrared (TIR) subsystem (Bands 10–14), atmospheric correction differs from that of the VNIR and SWIR subsystems due to the dominance of emissive rather than reflective radiance. Consequently, emissivity normalization was applied using the Emissivity Normalization (EN) algorithm [30]. This algorithm assumes that the minimum emissivity across bands approaches a constant value for each pixel, thereby isolating the spectral variability attributable to mineralogical composition rather than temperature.

In post-normalization, the TIR spectrum exhibits enhanced contrast between Bands 11–13, corresponding to Si–O stretching vibrations typical of quartz- and feldspar-bearing lithologies (Figure 6). This result aligns with findings from Rowan & Mars (2003), confirming that emissivity normalization effectively restores mineralogical information lost during raw TIR data acquisition [18].

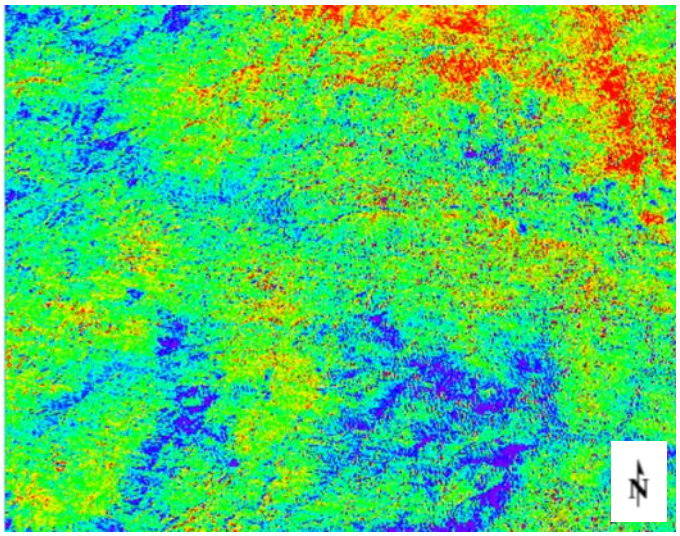

Figure 6. TIR emissivity spectrum before and after normalization for a silicate-rich pixel, showing improved spectral contrast among ASTER Bands 11–13

3.2.4. Layer Stacking and Integration

Upon completion of the atmospheric and emissivity corrections, the VNIR (Bands 1–3), SWIR (Bands 4–9), and TIR (Bands 10–14) datasets were merged into a single multiband composite image using the Layer Stack function. This integration facilitates subsequent PCA operations by ensuring spectral continuity and precise pixel alignment across all bands [23].

The merged composite image was visually inspected to ensure geometric alignment between the three subsystems. Residual band misalignments were corrected using the Image Registration (Warp) tool in ENVI, based on identifiable ground control points (GCPs).

The layer-stacked composite demonstrates distinct tonal variations corresponding to lithological differences in the study area. The enhanced clarity of the SWIR-dominated composite enables preliminary discrimination of alteration zones. Areas exhibiting high reflectance in Band 6 (2.205 μm) correlate with sericitic alteration, while moderate reflectance in Band 8 (2.33 μm) indicates propylitic zones (Figure 7).

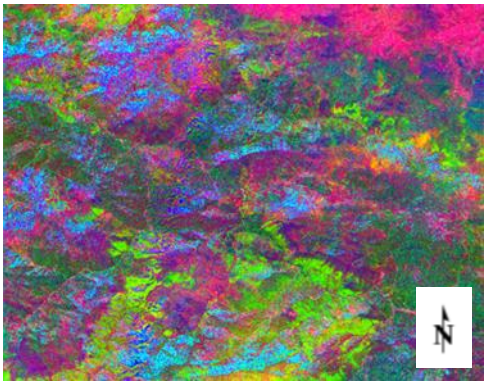

Figure 7. Layer-stacked false color composite (RGB: 4/6/8) showing the study area after preprocessing, highlighting improved radiometric balance and spectral clarity

3.2.5. Scientific Context

The preprocessing steps outlined above are critical for preserving the spectral fidelity of ASTER data and ensuring accurate mineralogical interpretation. The integration of IAR reflectance correction and emissivity normalization provides an effective balance between computational efficiency and spectral accuracy, particularly in mountainous terrains such as the Eastern Pontides, where variable topography and atmospheric thickness can induce significant reflectance distortions.

By following this sequence radiometric calibration, atmospheric correction, and subsystem integration the dataset becomes spectrally consistent and physically interpretable, satisfying the prerequisites for applying Principal

Component Analysis (PCA) to isolate hydrothermal alteration signatures. Comparable preprocessing frameworks have been validated in diverse geological settings, including the Meiduk area (Iran), the Oman Ophiolite Complex and the Singhbhum Shear Zone (India), confirming the robustness of this methodological approach [22-24].

3.3. Alteration Index Generation

Following preprocessing, a series of spectral alteration indices were generated from the ASTER imagery to enhance the diagnostic absorption features associated with key hydrothermal alteration minerals. Band ratio techniques were employed to derive these indices, enabling preliminary delineation of alteration zones before the application of Principal Component Analysis (PCA).

The use of band ratios minimizes illumination effects, enhances spectral contrast, and isolates diagnostic mineral absorption features in specific spectral regions [18, 19, 31]. This approach is particularly effective for multispectral sensors such as ASTER, where each band is sensitive to distinct mineralogical properties. The indices applied in this study were selected based on established methodologies from previous hydrothermal alteration studies [19, 29, 24].

The mathematical expressions and spectral rationale for the indices are summarized in Table 2, followed by graphical interpretations and figure analyses.

Table 2. ASTER-based alteration indices, their equations, spectral range, and associated mineral targets [21]

Alteration	Formula
Advanced Argillic Alt.	(B4+B6)/B5
Propylitization	(B6+B9)/(B7+B8)
Alunitization "ALI"	(B7/B5)*(B7/B8)
Kaolenization "KLI"	(B4/B5)*(B8/B6)
Argillic Alteration	(B5+B7)/B6
Fengitic Mica "Fengite"	B5/B6
Quartz Indice "QI"	(B11*B11)/(B10*B12)
Sericitization	(B5+B7)/B6

3.3.1 Al-OH (Hydroxyl-Bearing Minerals) Index

The Al–OH index targets minerals such as sericite, illite, and kaolinite, which exhibit prominent absorption near 2.2 μm due to Al–OH vibrational overtones. The ratio exploits ASTER's SWIR bands 5, 6, and 7:

$$\text{Al–OH Index} = \frac{B5 + B7}{B6}$$

where $5 = 2.165\,\mu m$, $B6 = 2.205\,\mu m$ and $B7 = 2.26\,\mu m$.

High index values correspond to strong Al–OH absorption and thus indicate zones of phyllic or argillic alteration dominated by sericite and kaolinite [29, 24].

The map reveals high Al–OH responses concentrated along the major NE–SW fault zones and intrusive contacts. These zones coincide spatially with quartz–sericite alteration halos mapped in field-based geological data (Figure 8-a). The spectral intensity and spatial clustering suggest active hydrothermal fluid pathways, consistent with phyllic alteration patterns reported in other segments of the Eastern Pontides [11].

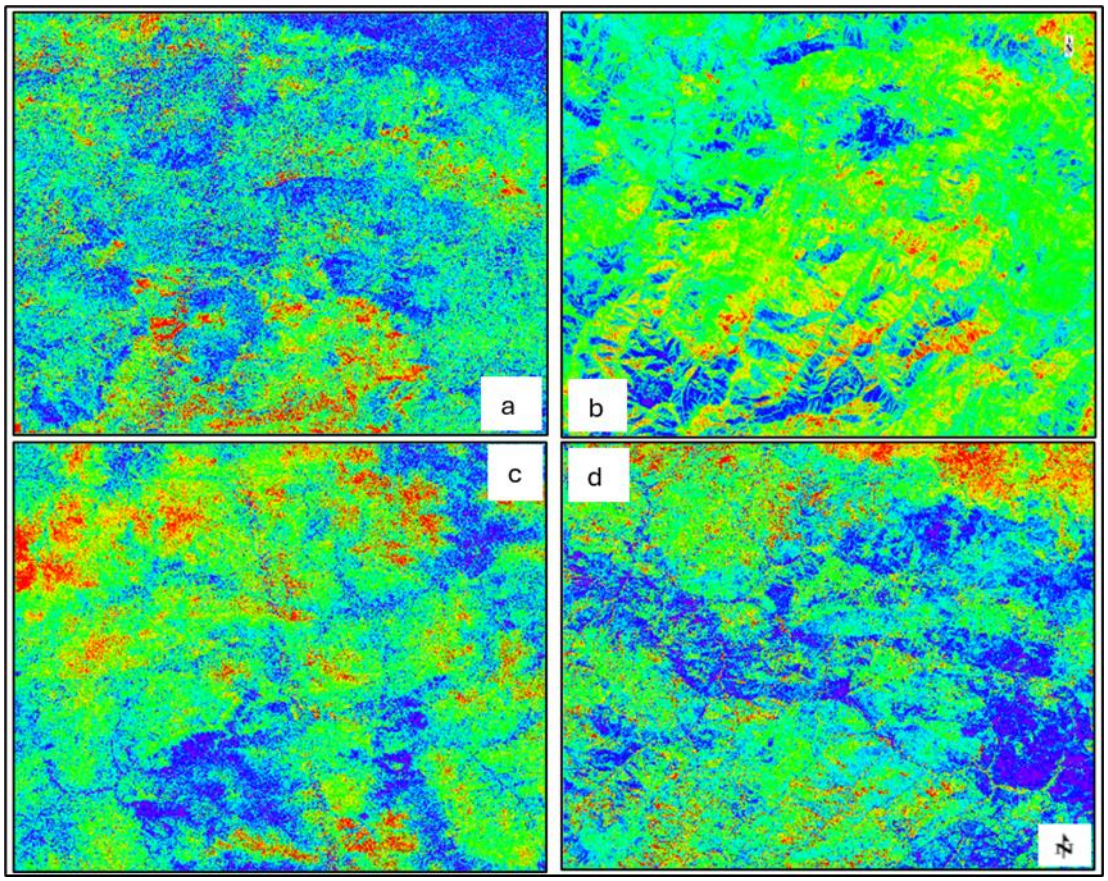

Figure 8. (a) Al–OH Index map derived from ASTER SWIR bands, showing spatial distribution of high hydroxyl absorption zones within the study area, **(b)** Fe–Oxide Index map showing ferric iron distribution across the study area, emphasizing oxidation zones and weathered alteration surfaces, **(c)** Mg–OH Index map highlighting chlorite–epidote–carbonate zones, **(d)** Silica Index map delineating quartz-rich and silicified zones in the study area

3.3.2 Fe-Oxide (Iron-Bearing Minerals) Index

The Fe–Oxide index enhances ferric minerals such as hematite, goethite, and limonite, which display diagnostic reflectance contrasts in the VNIR region. It is defined as:

$$\text{Fe–Oxide Index} = \frac{B2}{B1}$$

where $B1 = 0.56\,\mu m$ and $B2 = 0.66\,\mu m$.

Higher ratio values represent stronger ferric absorption, indicative of oxidation zones or gossanous alteration caps that often mark the uppermost portions of hydrothermal systems. Elevated Fe–Oxide index values occur predominantly in the central and western portions of the study area, where surficial oxidation and weathering processes are pronounced. The spatial correspondence between high Fe–Oxide zones and lithological contacts supports their interpretation as supergene alteration caps (Figure 8-b). Such zones may also delineate the oxidized tops of polymetallic systems, as observed in comparable PCA-based alteration studies [4, 19]

3.3.3 Mg-OH (Chlorite–Epidote) Index

The Mg–OH index focuses on absorption features around 2.33 μm, characteristic of chlorite, epidote, and carbonates. It is calculated using the following ratio:

$$\text{Mg–OH Index} = \frac{B8 + B9}{B7}$$

where $7 = 2.26\,\mu m$, $B8 = 2.33\,\mu m$ and $B9 = 2.395\,\mu m$.

High Mg–OH index values typically represent propylitic alteration zones, dominated by chlorite and epidote mineral assemblages, which form in the peripheral or distal regions of hydrothermal systems [23, 24].

The Mg–OH ratio map shows elevated responses along the southern and southeastern margins of the study area. These regions correspond to the outer alteration halo adjacent to tonalitic and granodioritic intrusions (Figure 8-c). The spectral pattern aligns with a propylitic alteration gradient, consistent with established alteration zonation models in porphyry–epithermal systems [32].

3.3.4 Silica (Si–O–H) Index

The Silica Index identifies quartz-rich and silicified zones through reflectance variations in VNIR bands sensitive to Si–O–H vibrations. It is defined as:

$$\text{Silica Index} = \frac{B4}{B2}$$

where $B4 = 1.65\,\mu m$ and $B2 = 0.66\,\mu m$.

Higher index values correspond to quartz and silicified outcrops, which often occur as core zones within hydrothermal alteration systems or as silicic veins associated with advanced argillic alteration [18, 19].

The silica ratio map indicates distinct high-reflectance anomalies in the central portion of the study area, coinciding with quartz–sericite alteration zones observed in the Al–OH map (Figure 8-a). The spectral correlation between these two indices suggests superimposed phyllic–silicic alteration, indicative of prolonged hydrothermal fluid evolution and multi-phase mineralization (Figure 8-d).

3.3.5 Advanced Argillic Alteration Index

To delineate advanced argillic alteration zones, characterized by minerals such as alunite and pyrophyllite, the following index was applied:

$$\text{Advanced Argillic Index} = \frac{B4 + B6}{B8}$$

where $4 = 1.65\,\mu m$, $B6 = 2.205\,\mu m$ and $B8 = 2.33\,\mu m$.

This index targets the absorption doublet near 2.17–2.20 µm, typical of Al–OH and SO_4-bearing phases [7, 24].

The Advanced Argillic map highlights strong responses in the northeastern sector of the study area, spatially associated with fault-controlled structures and hydrothermal breccia zones (Figure 9). The alignment of these anomalies with known structural conduits suggests that ascending acid-sulfate fluids contributed to advanced argillic mineral formation, a pattern analogous to high-sulfidation systems in other orogenic belts [8] [10].

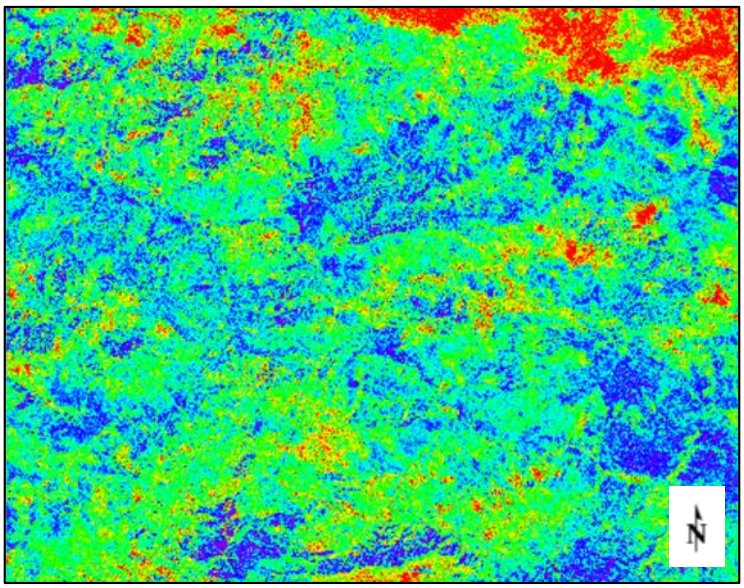

Figure 9. Advanced Argillic Alteration Index map showing high-alunite–pyrophyllite response zones

3.4. The Maxwell Colour Triangle and Its Application in Remote Sensing for Hydrothermal Alteration Detection

The Maxwell Colour Triangle represents the geometric formulation of James Clerk Maxwell's additive colour theory, illustrating how the primary light components (red (R), green (G), and blue (B)) combine in varying proportions to generate the continuum of perceivable colours [33]. Because contemporary digital remote sensing platforms use RGB-based visual encoding to represent multispectral reflectance, the triangle provides a conceptual framework for interpreting colour composites derived from satellite imagery [34, 35].

In hydrothermal alteration studies, the utility of this model becomes evident when specific spectral bands or diagnostic band ratios are mapped onto the RGB axes to emphasize mineralogical contrasts. Hydrothermal alteration assemblages express distinct spectral behaviours: iron oxides exhibit elevated reflectance in the visible red region; clay-rich minerals such as kaolinite, illite, and smectite possess well-defined absorption features in the SWIR domain; and silica-enriched zones frequently display subdued or spectrally neutral responses in the VNIR range [36, 37].

Assigning these diagnostic bands to the vertices of the Maxwell Triangle (through the red, green, and blue channels) produces colour clusters that correspond to specific alteration types. For example, Fe-oxide–rich surfaces are typically rendered in reddish tones, argillic alteration zones in greenish hues, and silicified units in bluish shades. This encoding strategy has been particularly effective in lithologic and alteration mapping with ASTER and Landsat datasets, enabling the detection of hydrothermal zonation with high spatial consistency [18].

Thus, the Maxwell Colour Triangle serves not only as a foundational construct of colour theory but also as a conceptual and operational instrument that facilitates the spectral-to-visual translation essential for remote identification of hydrothermal alteration systems (Figure 10).

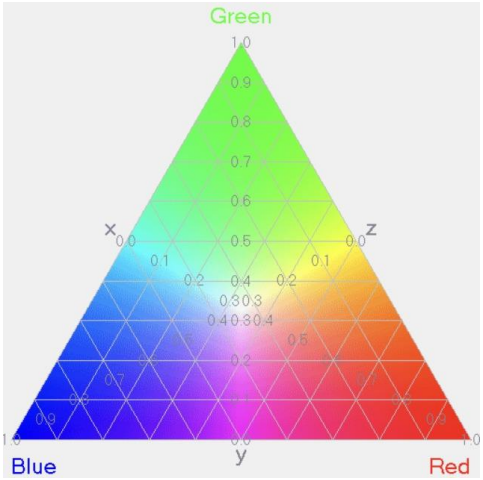

Figure 10. Maxwell Color Triangle [46]

3.5 Principal Component Analysis

3.5.1 Theoretical Background

Principal Component Analysis (PCA) is a multivariate statistical transformation that reorients correlated spectral data into a new set of orthogonal axes known as principal components (PCs) that successively maximize the variance within the dataset. The technique effectively compresses multispectral data into a reduced number of uncorrelated components while preserving the most significant spectral information [35, 36].

Mathematically, PCA operates on the variance–covariance matrix of the image data, decomposing it into its eigenvalues and eigenvectors:

$$\Sigma = \frac{1}{n-1}(X - \bar{X})^T(X - \bar{X})$$

where X is the matrix of pixel values for each band, $\bar{X}$ is the mean vector, and Σ is the covariance matrix.

The eigenvalue decomposition of Σ is then expressed as:

$$\Sigma e_i = \lambda_i e_i$$

where λ_i represents the eigenvalue corresponding to eigenvector e_i, which defines the direction of the new principal component axis. Each principal component (PC) image is computed as a linear combination of the original bands weighted by the eigenvector coefficients.

$$PC_i = X e_i$$

3.5.2 Implementation and Selective PCA Approach

In this study, PCA was implemented using ENVI 5.3, following radiometric and atmospheric corrections described in Section 3.2. To enhance mineral discrimination, PCA was performed selectively a technique referred to as Directional or Selective PCA where subsets of spectrally correlated bands (VNIR, SWIR, TIR) were analyzed independently.

Selective PCA offers two key advantages:

1. It reduces the dominance of broadband albedo effects found in full-spectrum PCA;
2. It allows isolation of wavelength-specific mineral absorption features, improving the detection of overlapping spectral responses [29, 23].

The following selective combinations were analyzed:

- VNIR (Bands 1–3): iron oxide and vegetation contrasts;
- SWIR (Bands 4–9): hydroxyl-bearing and clay minerals;
- TIR (Bands 10–14): silicate and carbonate compositions.

Each subset generated a new set of PCs, from which those exhibiting distinct spectral separation and high eigenvalue contrast were selected for visualization.
The RGB composite constructed from PC2 (R), PC3 (G), and PC4 (B) highlights hydrothermal alteration zones as distinct color anomalies (Figure 11).

- Reddish zones correspond to sericite-rich phyllic alteration,
- Greenish zones indicate quartz and silica-dominated areas, and
- Bluish regions represent kaolinite and advanced argillic assemblages.

The PCA composite effectively suppresses lithological background noise, enhancing spectral contrasts between mineralogical units. This spectral–spatial separation has been similarly documented by Fazli et al. (2019) in the Iranian Volcanic Belt and Vural and Aydal (2020) in the Eastern Pontides, confirming PCA's robustness for alteration mapping in complex geological settings [19, 39].

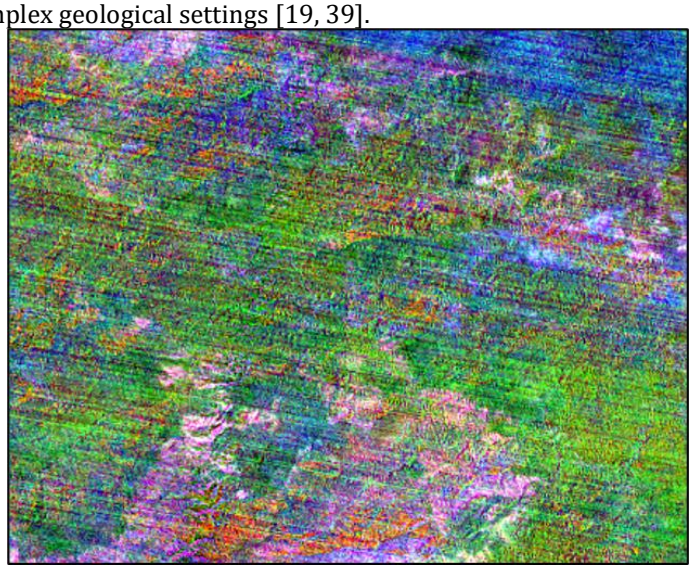

Figure 11. RGB composite map (PC2–PC3–PC4) generated from selective PCA of ASTER SWIR bands, emphasizing hydrothermal alteration zones

3.5.3 Eigenvalue and Component Selection

Eigenvalue analysis was used to identify which components contained the most relevant mineralogical information. The magnitude and sign of eigenvector loadings were examined to determine which bands contributed significantly to each component (Figure 12).

Eigenvectors	Band 1	Band 2	Band 3	Band 4	Band 5	Band 6	Band 7	Band 8
Band 1	-0.5404	-0.0093	-0.3186	-0.5404	0.0868	0.0135	0.0623	0.5503
Band 2	-0.2823	-0.0028	-0.0199	-0.2823	-0.6724	-0.3229	0.2342	-0.4785
Band 3	-0.0510	0.0193	-0.3635	-0.0510	-0.2913	0.6967	-0.4909	-0.2259
Band 4	0.1208	-0.0012	0.2380	0.1208	-0.4003	0.5142	0.6014	0.3575
Band 5	0.0036	0.0607	0.4948	0.0036	-0.4357	-0.1931	-0.5798	0.4337
Band 6	-0.0077	0.9979	-0.0201	-0.0077	0.0333	0.0009	0.0466	-0.0205
Band 7	-0.3332	-0.0084	0.6812	-0.3332	0.3228	0.3293	-0.0136	-0.3177
Band 8	-0.7071	-0.0000	0.0000	0.7071	0.0000	0.0000	-0.0000	-0.0000

Figure 12. Eigenvalues indicate which bands should be used in PCA analysis. The largest value corresponding to each band is selected and interpretations are performed.

3.5.4. Scientific Implications

The PCA-based analysis confirms that statistical separation of multispectral data can effectively isolate overlapping spectral signatures associated with hydrothermal alteration minerals. Compared to traditional band ratio methods, PCA reduces redundancy, enhances subtle mineralogical variations, and provides quantitative evidence for zonal alteration.

This methodological framework aligns with and extends previous works that utilized ASTER–PCA integration for mineral exploration [4, 19, 24]. The selective PCA approach employed here focusing on spectrally relevant subsets proves particularly effective in complex geological settings where multiple alteration assemblages coexist.

Consequently, the PCA results form the analytical foundation for quantitative interpretation and validation, which are presented in the subsequent Results section.

4. Discussions

The Principal Component Analysis (PCA) applied to ASTER multispectral data effectively distinguished hydrothermal alteration zones within the Aktutan region, revealing a strong correlation between spectral anomalies and geological structures. The eigenvalue analysis indicated that the first three principal components captured the majority of spectral variance, while subsequent components highlighted mineral-specific absorptions, particularly within the SWIR range. These spectral behaviors, notably the negative loadings in Band 6 (2.205 μm) and positive loadings in Band 8 (2.33 μm), are consistent with the diagnostic absorption of sericite and chlorite, respectively, validating the selective PCA approach in isolating hydrothermal minerals.

The final alteration zonation map (Figure 13) illustrates three distinct alteration domains (silicic, kaolinite-rich, and advanced argillic) forming a concentric spatial pattern around magmatic and structural centers. The central silicic–phyllic core represents high-temperature mineralization, while the peripheral zones of kaolinite and advanced argillic alteration indicate successive cooling and acid-sulfate conditions. The close spatial correspondence of these alteration zones with NE–SW-trending faults and intrusive contacts emphasizes the structural control on hydrothermal fluid migration. Such zonation aligns well with classical porphyry–epithermal models described by Sillitoe (2010) and comparable PCA-based studies in the Eastern Pontides [19, 24, 32, 39-44].

The high coherence between PCA results and band ratio indices confirms that PCA provides enhanced spectral discrimination by minimizing redundancy and emphasizing diagnostic absorption features. This statistical robustness enables the delineation of overlapping alteration assemblages that are often difficult to separate using conventional band ratio techniques alone. The findings validate the applicability of PCA as a cost-effective, transferable approach for identifying hydrothermal systems in geologically complex terrains. Consequently, the PCA-based workflow developed in this study contributes a reproducible methodology for regional mineral exploration, highlighting the potential of ASTER data in structural and alteration mapping within orogenic belts.

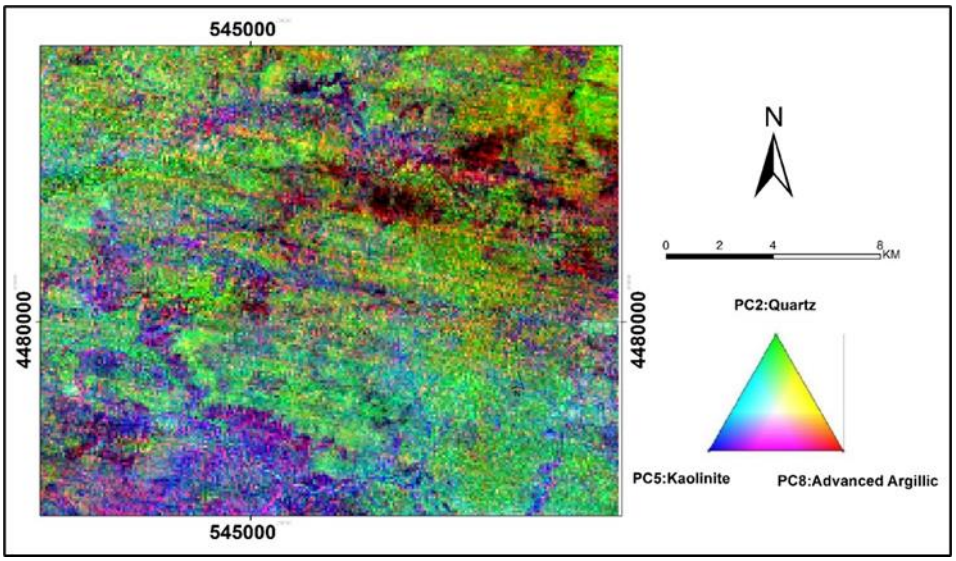

Figure 13. Final alteration zonation map derived from integrated PCA and band ratio analysis, illustrating the concentric distribution of alteration types within the study area

The final alteration map delineates three major alteration zones (Quartz, Kaolinite, Advanced argillic) with well-defined spatial boundaries. These results demonstrate the efficacy of PCA in distinguishing overlapping spectral responses and emphasize the potential of ASTER-based multispectral analysis for regional mineral exploration in complex tectonic terrains.

5. Conclusion

This study demonstrates the efficiency of Principal Component Analysis (PCA) applied to ASTER multispectral data in identifying and characterizing hydrothermal alteration zones within the Aktutan region, situated in the tectonically complex Eastern Pontides Orogenic Belt. Through rigorous preprocessing, radiometric calibration, and atmospheric correction, the spectral integrity of VNIR, SWIR, and TIR data was successfully preserved, enabling the isolation of key mineralogical assemblages using a selective PCA approach.

The results confirm that PCA provides superior spectral discrimination compared to conventional band ratio methods by reducing data redundancy and enhancing subtle mineralogical contrasts. The eigenvalue analysis and subsequent component selection effectively distinguished absorption features associated with hydroxyl- and silica-bearing minerals, including sericite, kaolinite, and chlorite. The final PCA-derived alteration map (Figure 14) delineates a clear concentric zonation pattern consisting of central silicic–phyllic cores surrounded by peripheral argillic and propylitic envelopes, spatially controlled by NE–SW-trending fault systems and magmatic intrusions. This distribution validates the structural influence on hydrothermal processes and reflects the typical mineralogical succession of porphyry–epithermal systems.

Methodologically, the selective PCA applied to ASTER data in this study demonstrates a reproducible and cost-effective framework for hydrothermal alteration mapping in geologically intricate terrains. Regionally, the results contribute to refining the understanding of mineralization controls within the Eastern Pontides, offering a remote sensing–based tool that can complement field-based exploration. Future studies should integrate hyperspectral datasets, field spectroscopy, and machine learning based classification techniques to improve mineral discrimination accuracy and enable automated mapping across broader orogenic domains.

Author Contribution

Mustafa Ceylan – Conceptualization, methodology, supervision, resources, data collection and processing, analysis, literature review, writing – original draft preparation, and review and editing.

Gökhan Külekçi – Supervision, resources, writing – review and editing.

Conflict of Interest

The authors confirm that there is no known conflict of interest or common interest with any institution/organization or person.

References

[1] El-Hadidy, S. M., & Youssef, M. A. S. (2024). Exploring geothermal energy prospects through radioelement enrichment zones in Gabal Abu Hashim area in southeastern Aswan by geophysical and remote sensing data integration. Scientific Reports, 14, 77393. https://doi.org/10.1038/s41598-024-77393-8

[2] Hegab, M. A. E. R., & Abou El Magd, I. (2024). Revealing potential mineralization zones utilizing Landsat-9, ASTER and airborne radiometric data at Elkharaza–Dara Area, Northeastern Desert, Egypt. The Egyptian Journal of Remote Sensing and Space Sciences, 27(4), 100–114. https://doi.org/10.1016/j.ejrs.2024.10.005

[3] Martial, F. E., Ousmanou, S., & Madeleine, N. M. (2025). Mapping and discrimination of the mineralization potential in the Bonako area (Central Cameroon Domain): Insights from Landsat 9 OLI data, GIS fuzzy modeling techniques and field observations. Geosystems and Geoenvironment. https://doi.org/10.1016/j.geogeo.2024.100347

[4] Vural, A., Akpinar, İ., Sipahi, F., (2021). Mineralogical and Chemical Characteristics of Clay Areas, Gümüşhane Region (NE Turkey), and Their Detection Using the Crósta Technique with Landsat 7 and 8 Images. Natural Resources Research, 30, 3955–3985.

[5] Liu, Q., Ye, Z., Zhu, C., Ouyang, D., Gu, D., & Wang, H. (2025). Intelligent Target Detection in Synthetic Aperture Radar Images Based on Multi-Level Fusion. Remote Sensing, 17(1), 112. https://doi.org/10.3390/rs17010112

[6] Seifi, A., Yousefi, S., Aryafar, A., & Hosseinjanizadeh, M. (2025). Evaluation of decision tree on ASTER statistical data for segregating alteration zones in Darrehzar deposit, Iran. Earth Science Informatics. https://doi.org/10.1007/s12145-025-01984-w

[7] Kalimuthu, R., Porwal, A., & Pandalai, H. S. (2025). Remote mapping of lineaments and hydrothermal alteration zones related to unconformity-related uranium deposits in the Badami Group of the Western Kaladgi Basin, India. Ore and Energy Resource Geology. https://doi.org/10.1016/j.oreoa.2025.100106

[8] Akinlalu, A. A. (2025). Exploration of iron ore deposits in parts of Kogi State, northcentral Nigeria: Analyses from airborne magnetic and ASTER datasets. Geosystems and Geoenvironment. https://doi.org/10.1016/j.geogeo.2025.100359

[9] Olomo, K. O., Mohammed, M. Z., & Olomo, O. K. (2025). Multispectral remote sensing expression of lineaments and alteration minerals in part of crystalline rock units of Southwestern Nigeria: Implication on gold prospecting. Ore and Energy Resource Geology. https://doi.org/10.1016/j.oreoa.2025.100091

[10] Yousif, T. M., Aromolaran, O. K., & Kheiralla, K. M. (2025). Lineaments and hydrothermal alteration mapping in the Arkawit area, Northeastern Sudan: Insights from remote sensing. Arabian Journal of Geosciences. https://doi.org/10.1007/s12517-025-12222-4

[11] Vural, A., & Kaya, A. (2020). Study on the natural and artificial radioactivity risk of the Aktutan alteration site (Gümüşhane). In Proceedings of the 5th International Congress of Health Sciences and Management (5. Uluslararası Sağlık Bilimleri ve Yönetimi Kongresi), Kırşehir, Turkey.

[12] Vural, A. (2024). The relationship between hydrothermal alteration and element accumulation in Sessile Oak (Quercus petraea L.): A case study from the Canca hydrothermal alteration zone (Gümüşhane, Türkiye). Turkish Journal of Analytical Chemistry, 9(1), 45–56. https://doi.org/10.51435/turkjac.1494920

[13] Akinlalu, A. A. (2025). Exploration of iron ore deposits in parts of Kogi State, northcentral Nigeria: Analyses from airborne magnetic and ASTER datasets. Geosystems and Geoenvironment. https://doi.org/10.1016/j.geogeo.2025.100359

[14] Kalimuthu, R., Porwal, A., & Pandalai, H. S. (2025). Remote mapping of lineaments and hydrothermal alteration zones related to unconformity-related uranium deposits in the Badami Group of the Western Kaladgi Basin, India. Ore and Energy Resource Geology. https://doi.org/10.1016/j.oreoa.2025.100106

[15] Bai, Y., Wang, J., Jiang, G., Zhou, K., Zhou, S., Mi, W., & An, Y. (2025). Identification of alteration minerals and lithium-bearing pegmatite deposits using remote sensing satellite data in Dahongliutan area, Western Kunlun, NW China. Minerals, 15(7), 671. https://doi.org/10.3390/min15070671

[16] El-Hadidy, S. M., & Youssef, M. A. S. (2024). Exploring geothermal energy prospects through radioelement enrichment zones in Gabal Abu Hashim area in southeastern Aswan by geophysical and remote sensing data integration. Scientific Reports, 14, 77393. https://doi.org/10.1038/s41598-024-77393-8

[17] Yamaguchi, Y., Kahle, A. B., Tsu, H., Kawakami, T., & Pniel, M. (1998). Overview of Advanced Spaceborne Thermal Emission and Reflection Radiometer (ASTER). IEEE Transactions on Geoscience and Remote Sensing, 36(4), 1062–1071. https://doi.org/10.1109/36.700991

[18] Rowan, L. C., & Mars, J. C. (2003). Lithologic mapping in the Mountain Pass, California area using Advanced Spaceborne Thermal Emission and Reflection Radiometer (ASTER) data. Remote Sensing of Environment, 84(3), 350–366. https://doi.org/10.1016/S0034-4257(02)00127-X

[19] Fazli, S., Taghipour, B., Moore, F., & Lentz, D. R. (2019). Fluid inclusions, S isotopes, and Pb isotopes characteristics of the Kuh-e-Surmeh carbonate-hosted Zn–Pb deposit in the Zagros Fold Belt, southwest Iran: Implications for the source of metals and sulfur and MVT genetic model. Ore Geology Reviews, 109, 615–629. https://doi.org/10.1016/j.oregeorev.2019.04.006

[20] Hegab, M. A. E. R., & Abou El Magd, I. (2024). Revealing potential mineralization zones utilizing Landsat-9, ASTER and airborne radiometric data at Elkharaza–Dara Area, Northeastern Desert, Egypt. The Egyptian Journal of Remote Sensing and Space Sciences, 27(4), 100–114. https://doi.org/10.1016/j.ejrs.2024.10.005

[21] Rajan Girija, R., & Mayappan, S. (2019). Mapping of mineral resources and lithological units: a review of remote sensing techniques. International Journal of Image and Data Fusion, 10(2), 79–106. https://doi.org/10.1080/19479832.2019.1589585

[22] Olomo, K. O., Mohammed, M. Z., & Olomo, O. K. (2025). Multispectral remote sensing expression of lineaments and alteration minerals in part of crystalline rock units of Southwestern Nigeria: Implication on gold prospecting. Ore and Energy Resource Geology. https://doi.org/10.1016/j.oreoa.2025.100091

[23] Vural, A. (2015). Assessment of metal pollution associated with an alteration area: Old Gümüşhane, NE Black Sea. Environmental Science and Pollution Research, 22(5), 3219–3228. https://doi.org/10.1007/s11356-014-2907-7

[24] Fathi, A., Lee, T. & Mohebzadeh, H. Allocating Underground Dam Sites Using Remote Sensing and GIS Case Study on the Southwestern Plain of Tehran Province, Iran. Journal of the Indian Society of Remote Sensing, 47, 989–1002 (2019). https://doi.org/10.1007/s12524-019-00961-3

[25] Chavez, P. S. (1988). An improved dark-object subtraction technique for atmospheric scattering correction of multispectral data. Remote Sensing of Environment, 24(3), 459–479. https://doi.org/10.1016/0034-4257(88)90019-3

[26] Clark, R. N., Swayze, G. A., Gallagher, A. J., King, T. V. V., & Calvin, W. M. (2003). The U.S. Geological Survey Tetracorder and expert systems for imaging spectroscopy. Journal of Geophysical Research: Planets, 108(E12). https://doi.org/10.1029/2002JE001847

[27] Yousif, T. M., Aromolaran, O. K., & Kheiralla, K. M. (2025). Lineaments and hydrothermal alteration mapping in the Arkawit area, Northeastern Sudan: Insights from remote sensing. Arabian Journal of Geosciences. https://doi.org/10.1007/s12517-025-12222-4

[28] Vural, A. (2015). Assessment of metal pollution associated with an alteration area: Old Gümüşhane, NE Black Sea. Environmental Science and Pollution Research, 22(5), 3219–3228. https://doi.org/10.1007/s11356-014-2907-7

[29] Külekçi, G. (2024). Madencilik Operasyonlarında Segmentasyon Teknolojileri: Uydu ve Dron Verilerinden Bilgi Çıkarmada Derin Öğrenme Yaklaşımları. International Journal of Advanced Natural Sciences and Engineering Researches, 8(11), 732-740.

[30] Gillespie, A. R., Rokugawa, S., Matsunaga, T., Cothern, J. S., Hook, S. J., & Kahle, A. B. (1998). A temperature and emissivity separation algorithm for Advanced Spaceborne Thermal Emission and Reflection Radiometer (ASTER) images. IEEE Transactions on Geoscience and Remote Sensing, 36(4), 1113–1126. https://doi.org/10.1109/36.700995

[31] Martial, F. E., Ousmanou, S., & Madeleine, N. M. (2025). Mapping and discrimination of the mineralization potential in the Bonako area (Central Cameroon Domain): Insights from Landsat 9 OLI data, GIS fuzzy modeling techniques and field observations. Geosystems and Geoenvironment. https://doi.org/10.1016/j.geogeo.2024.100347

[32] Sillitoe, R. H. (2010). Porphyry copper systems. Economic Geology, 105(1), 3–41. https://doi.org/10.2113/gsecongeo.105.1.3

[33] Maxwell, J. C. (1860). On the Theory of Compound Colours, and the Relations of the Colours of the Spectrum. Philosophical Transactions of the Royal Society of London, 150, 57–84. https://doi.org/10.1098/rstl.1860.0005

[34] Vural, A. (2015). Contamination assessment of heavy metals associated with an alteration area: Demirören, Gümüşhane, NE Turkey. Journal of the Geological Society of India, 86(2), 215–222. https://doi.org/10.1007/s12594-015-0301-9

[35] Salem, I. A. N., Kamh, S. Z., & Saleh, G. M. (2024). Enhanced geological and radioactive mapping of Gabal Abu Ashayir-Gabal El Bakriyah area, central Eastern Desert, Egypt, using remotely sensing data. Journal of Umm Al-Qura University for Applied Sciences. https://doi.org/10.1007/s43994-024-00194-2

[36] Hunt, G. R. (1977). Spectral signatures of particulate minerals in the visible and near infrared. Geophysics, 42(3), 501–513. https://doi.org/10.1190/1.1440721

[37] Lillesand, T. M., Kiefer, R. W., & Chipman, J. W. (2015). Remote Sensing and Image Interpretation (7th ed.). Wiley.

[38] Vural, A., 2024. Soil geochemistry survey for gold exploration at Kısacık area (Çanakkale, Ayvacık, Türkiye). Periodico di Mineralogia, 93 (2), 61-83" and " Vural A (2017). Gold and Silver Content of Plant Helichrysum Arenarium, Popularly Known as the Golden Flower, Growing in Gümüshane, NE Turkey. Acta Physica Polonica A, 132(3-II), 978-980., Doi: 10.12693/APhysPolA.132.978

[39] Vural, A., & Aydal, D. (2020). Determination of lithological differences and hydrothermal alteration areas by remote sensing studies: Kısacık (Ayvacık-Çanakkale, Biga Peninsula, Turkey). Journal of Engineering Research and Applied Science, 9(1), 1341–1357.

[40] Vural, A., Çorumluoğlu, Ö., & Asri, İ. (2017). Remote sensing technique for capturing and exploration of mineral deposit sites in Gümüşhane metallogenic province, NE Turkey. Journal of the Geological Society of India, 90(5), 628–633. https://doi.org/10.1007/s12594-017-0762-0

[41] Seifi, A., Yousefi, S., Aryafar, A., & Hosseinjanizadeh, M. (2025). Evaluation of decision tree on ASTER statistical data for segregating alteration zones in Darrehzar deposit, Iran. Earth Science Informatics. https://doi.org/10.1007/s12145-025-01984-w

[42] Vural, A. (2015). Contamination assessment of heavy metals associated with an alteration area: Demirören, Gümüşhane, NE Turkey. Journal of the Geological Society of India, 86(2), 215–222. https://doi.org/10.1007/s12594-015-0301-9

[43] Vural, A., & Kaya, A. (2020). Study on the natural and artificial radioactivity risk of the Aktutan alteration site (Gümüşhane). In Proceedings of the 5th International Congress of Health Sciences and Management (5. Uluslararası Sağlık Bilimleri ve Yönetimi Kongresi), Kırşehir, Turkey.

[44] Vural, A (2015). Biogeochemical characteristics of Rosa canina grown in hydrothermally contaminated soils of the Gümüşhane province, Northeast Turkey. Environmental Monitoring and Assessment. 187, 486. Doi. 10.1007/s10661-015-4708-y

[45] Satellite Imaging Corporation. (n.d.). ASTER (Advanced Spaceborne Thermal Emission and Reflection Radiometer). Retrieved December 9, 2025, from https://www.satimagingcorp.com/satellite-sensors/other-satellite-sensors/aster/

[46] Reid, J. S. (n.d.). James Clerk Maxwell's triumphant legacy. University of Aberdeen. Retrieved December 9, 2025, from https://homepages.abdn.ac.uk/j.s.reid/pages/Maxwell/Legacy/MaxTri.html